scientific reports

Check for updates

OPEN

Densification of hydroxyapatite/zirconia nanocomposites fabricated via low-temperature mineralization sintering process and their mechanical properties

Yeongjun Seo[1]✉, Shiori Nawa[1], Tomoyo Goto[1,2], Sunghun Cho[1] & Tohru Sekino[1]✉

Hydroxyapatite/zirconia (HAP/ZrO_2) composites were fabricated via the low-temperature mineralization sintering process (LMSP) at an extremely low temperature of 130 °C to enhance the mechanical properties of HAP and broaden its practical applications. For this purpose, 5–20 vol% calcia-stabilized ZrO_2 were introduced into HAP, and HAP/ZrO_2 nanoparticles, mixed with simulated body fluid, were densified under a uniaxial pressure of 800 MPa at 130 °C. At 10 vol% ZrO_2, the relative density of the HAP/ZrO_2 composite was determined to be 88.3 ± 1.1%. Additionally, it exhibited the highest values of mechanical properties such as the Vickers hardness (3.68 ± 0.18 GPa), fracture toughness (1.11 ± 0.10 MPa·$m^{1/2}$), biaxial flexural strength (63.72 ± 2.35 MPa), and Young's modulus (83.91 ± 1.93 GPa) among the composite samples. These values were considerably higher than those of the pure HAP matrix due to the adequate reinforcement by ZrO_2 nanoparticles. Notably, owing to the low sintering temperature, phase decomposition of HAP, normally observed at high sintering temperatures above 1200 °C, was not observed. These results suggest that LMSP enables the incorporation of reinforcing ceramic materials with high sintering temperatures into bioactive materials at significantly lower temperatures, thereby improving their properties.

Keywords Biomineralization, Cold sintering process, Hydroxyapatite, Zirconia, Mechanical properties, Low-temperature sintering

Hydroxyapatite (HAP, $Ca_{10}(PO_4)_6(OH)_2$) constitutes the primary inorganic component of human bones and teeth. It bonds directly with hard tissues due to its excellent biocompatibility and bioactivity[1,2]. These unique properties are conducive to its utilization in various biomedical fields including bone tissue engineering, dental implants, orthopedic implants, and drug delivery systems[2–4]. However, as HAP exhibits poor mechanical properties, it has been primarily utilized in areas where mechanical strength requirements are not as stringent, e.g., for implant coatings and non-load-bearing implants[5,6]. Therefore, to broaden the use of HAP in biomedical applications, the main challenge is to enhance its mechanical properties closer to those of living bone.

Incorporation of reinforcing phases into a base material is one of the effective methods to improve its properties beyond those that can be achieved by individual materials. To improve the mechanical properties of HAP, metal and ceramic materials are generally introduced into HAP rather than polymeric materials because they can directly affect the strength and toughness[7]. However, there are several problems for utilization of metallic materials in the human body owing to their corrosion, wear, and high stiffness[7,8]. Therefore, ceramics such as alumina (Al_2O_3), zirconia (ZrO_2), and titania (TiO_2) have commonly been introduced into HAP as reinforcing materials to enhance the strength and toughness[9–11]. Among these materials, ZrO_2 is very promising as a representative bioinert material that exhibits excellent mechanical properties, biocompatibility, resistance to corrosion, and low toxicity, and thus is ideal for applications such as dental and orthopedic implants, dental crowns, and medical devices[10,12–15]. However, owing to the high sintering temperatures of ZrO_2, typically ranging from 1200 to 1500 °C, it is difficult to fabricate dense HAp/ZrO_2 composites[16,17]. Additionally, within this temperature range, HAP undergoes thermal instability, leading to phase decomposition into β-tricalcium

[1]SANKEN, Osaka University, 8–1 Mihogaoka, Ibaraki 567–0047, Osaka, Japan. [2]Institute for Advanced Co-Creation Studies, Osaka University, 1–1 Yamadaoka, Suita 565–0871, Osaka, Japan. ✉email: yjseo@sanken.osaka-u.ac.jp; sekino@sanken.osaka-u.ac.jp

phosphate (β-TCP), oxyapatite ($Ca(PO_4)_6O$), and CaO[16–18]. Owing to these reasons, HAP/ZrO_2 composites have been widely investigated using various sintering methods[19–21]. To address these challenges, nanoscale ZrO_2 particles and careful control of the added amount of ZrO_2 have been employed[19]. Additionally, spark plasma sintering[20] and hot isostatic pressing[21] have been utilized to suppress phase decomposition by reducing the sintering temperature and time and creating a hermetic environment, respectively. Nevertheless, these sintering techniques still entail high sintering temperatures, leading to an increased energy consumption, significant preparation costs, and emissions of gases.

Recently, a novel sintering technique, referred to as cold sintering process (CSP), has been reported[22]. CSP can be used to densify inorganic particles at extremely low temperatures below 300 °C. The densification mechanism of CSP is quite different from that of the conventional sintering process. The main driving force in CSP is a transient liquid phase, which dissolves the inorganic base materials and subsequently moves into the vacant areas between the particles by a chemical potential gradient[22–24]. Through this mass transport, the dissolved components are precipitated, filling the vacant areas under a hydrothermal-like environment. Based on the CSP mechanism combined with biomineralization, we have demonstrated the low-temperature densification of bioactive glass and HAP nanoparticles[25,26]. This process, called the low-temperature mineralization sintering process (LMSP), allows apatite-like crystals to precipitate at particle boundaries under pseudo-biomineralization induced by simulated body fluid (SBF) during densification. Particularly, in the case of HAP nanoparticles, transparent HAP ceramics with a relative density of over 98% and transmittance of 80% in the visible light range were obtained via LMSP at a sintering temperature below 200°C[26]. This was realized because the introduction of SBF successfully triggered the precipitation of a new HAP phase between the base HAP nanoparticles, leading to the final densification. Thus, utilizing LMSP, even dense HAP/ZrO_2 composites can be fabricated at significantly lower temperatures and under environmentally friendly conditions compared to other sintering techniques. Additionally, the low sintering temperature can help prevent the formation of unexpected phases due to phase decomposition observed in the high-temperature sintering process.

In this study, we carried out a low-temperature densification of HAP/ZrO_2 composites using LMSP. To induce biomineralization during LMSP, an SBF solution was introduced into HAP/ZrO_2 mixed powders. As the bioactivity of ZrO_2 is limited compared to HAP, a large amount of ZrO_2 is less likely to facilitate the precipitation of the HAP phase by reacting with the SBF solution within a short sintering time, possibly resulting in a degradation in densification[27]. Therefore, we focused on the volume fraction of ZrO_2 that can improve the mechanical properties with a high densification in the HAP matrix. For this purpose, the densification conditions were optimized with control of sintering pressures and times, and the relative densities of HAP/ZrO_2 composites with different amounts of ZrO_2 were examined. Additionally, microstructural features and phase transformation of the composites were evaluated. Finally, the mechanical properties such as Vickers hardness, fracture toughness, biaxial flexural strength, and Young's modulus of the composites were investigated, and the changing behaviors against the volume fraction of ZrO_2 are discussed in detail.

Methods

Synthesis of HAP nanoparticles

HAP nanoparticles were synthesized by a wet precipitation method[28,29]. A calcium solution (5 M) and a phosphate solution (3 M), prepared from calcium nitrate tetrahydrate (FUJIFILM Wako Pure Chemical Corp., Osaka, Japan) and ammonium dibasic phosphate (FUJIFILM Wako Pure Chemical Corp., Osaka, Japan), respectively, were mixed with a control of the pH at 10.5 ± 0.2 using an ammonia solution (FUJIFILM Wako Pure Chemical Corp., Osaka, Japan). After mixing for 1 h, the mixture was aged for 12 h at room temperature. Subsequently, the precipitate was obtained after washing by filtration with an ultrapure water, and then dried in an oven at 110 °C.

LMSP of HAP/ZrO_2 composites

The obtained HAP nanoparticles were mixed with calcia-stabilized ZrO_2 nanoparticles (4.4 mol% CaO, Daiichi Kigenso Kagaku Kogyo Co., Ltd., Osaka, Japan) at 5, 10, 15, and 20 vol% using a planetary mill in absolute ethanol (FUJIFILM Wako Pure Chemical Corp., Osaka, Japan), employing a ZrO_2 jar and balls at a rotation speed of 300 rpm for 3 h. Subsequently, HAP/ZrO_2 nanoparticles were separated from the absolute ethanol by an evaporator, and then thoroughly dried in the oven at 60 °C overnight. For the densification, 0.4 g of the HAP/ZrO_2 nanoparticles was mixed with a 20 wt% SBF solution (0.08 g), synthesized by the Kokubo's method[30]. The ion concentration of SBF solution is listed in Table 1. The mixture was placed into a cylindrical mold with a diameter of 12 mm and then heated at 130 °C under uniaxial pressures (200–800 MPa) for 10–120 min. For comparison, raw calcia-stabilized ZrO_2 nanoparticles mixed with 20 wt% SBF solution were also heated at 130 °C under uniaxial pressure of 800 MPa for 120 min. After heating and pressing, the sintered HAP/ZrO_2 composites were dried in the oven at 110 °C to remove the residual solution.

Ion	Na^+	K^+	Mg^{2+}	Ca^{2+}	Cl^-	HCO_3^-	HPO_4^{2-}	SO_4^{2-}
Human blood plasma	142.0	5.0	1.5	2.5	103.0	27.0	1.0	0.5
SBF	142.0	5.0	1.5	2.5	148.8	4.2	1.0	0.5

Table 1. Ion concentration (mmol/L) of human blood plasma and SBF solution.

Characterization

The morphologies of the synthesized HAP and as-received ZrO_2 nanoparticles were observed using field-emission scanning electron microscopy (FE-SEM, SU9000, Hitachi High-Tech Corp., Tokyo, Japan). Additionally, their phases were examined using X-ray diffraction (XRD, D8 Advance, Bruker AXS GmbH, Karlsruhe, Germany) with Cu Kα radiation ($\lambda = 1.54178$ Å) at 40 kV and 40 mA. The bulk densities of the HAP/ZrO_2 composites were estimated using the Archimedes' method. Absolute ethanol was employed as a liquid medium. The fracture surfaces of the composites were observed by FE-SEM. Transmission electron microscopy with energy-dispersed X-ray spectroscopy (TEM-EDX, JEM-ARM200F, JEOL Ltd., Tokyo, Japan) was utilized to further distinguish the crystalline structure and distribution between HAP and ZrO_2. The phase transformation during LMSP of the composites was observed by XRD. Moreover, based on the XRD results, monoclinic intensity ratio (MIR) was evaluated to estimate the fractions of tetragonal ZrO_2 (t-ZrO_2) and monoclinic ZrO_2 (m-ZrO_2) in the composites by[31,32]

$$\mathrm{MIR}\,(\%) = \frac{\left\{\mathrm{I_m}\left(\bar{1}11\right) + \mathrm{I_m}\,(111)\right\}}{\left\{\mathrm{I_m}\left(\bar{1}11\right) + \mathrm{I_t}\,(111) + \mathrm{I_m}\,(111)\right\}} \times 100 \tag{1}$$

where I indicates the peak intensity for each lattice plane and the subscripts m and t represent monoclinic and tetragonal, respectively. Based on the MIR results, we assumed the final compositions (HAP: t-ZrO_2:m-ZrO_2)of the composites and calculated their theoretical densities using the rule of mixtures ($\rho_{HAP} = 3.16$ g/cm^3, $\rho_{t-ZrO2} = 6.04$ g/cm^3, and $\rho_{m-ZrO2} = 5.78$ g/cm^3). For the mechanical properties of the composites, their Vickers hardnesses were measured using a Vickers hardness tester (FV-310e, Future-Tech Corp., Kanagawa, Japan) under an applied load of 9.8 N and holding time of 15 s. Under the same conditions, the fracture toughness (K_{IC}) was calculated using the indentation fracture method with the following equation[33]:

$$\mathrm{K_{IC}} = 0.203\,(\mathrm{c/a})^{-3/2}\,\mathrm{H_v a^{1/2}} \tag{2}$$

where c is half of the crack length, a is half of the indentation diagonal length, and H_v is the measured Vickers hardness. The biaxial flexural strength was estimated using a piston-on-three-balls test with a universal testing machine (AGX-10kNVD, Shimadzu Corp., Kyoto, Japan) equipped with a 5 kN load cell. The Young's modulus was evaluated using the ultrasonic velocity observed by a digital storage oscilloscope (DSOX3052T, Keysight, Tokyo, Japan) and ultrasonic pulser/receiver (Model 5072, PANAMETRICS, MA, USA). All these mechanical properties of each sample were measured at least six times, and the average values are presented.

Results and discussion

Densification and microstructures of HAP/ZrO_2 composites

As shown in Fig. 1, HAP nanoparticles were synthesized by a wet precipitation method, represented by a single phase of HAP in an XRD pattern corresponding to PDF card no. 00–009–0432. Additionally, the calcia-stabilized ZrO_2 nanoparticles were composed mainly of a tetragonal phase.

To optimize the densification conditions, HAP/ZrO_2 mixed nanoparticles with 5 vol% ZrO_2 were mixed with a 20 wt% SBF solution and subsequently densified at 130 °C under various uniaxial pressures and sintering times (Fig. 2). Theoretical densities and relative densities of all the composites are provided in Table S1. As shown in Fig. 2a, with the increase in the pressure and a sintering time of 30 min, the relative density of the composites was gradually improved from 83.0 ± 1.4% to 86.0 ± 0.8% of the theoretical densities calculated by the rule of mixtures. This increase can be attributed to the higher uniaxial pressure, which can affect the improved particle sliding and rearrangement, resulting in a higher packing density[22,34]. While varying the sintering time with the pressure maintained at the optimized value of 800 MPa, the relative density increased as the sintering was prolonged and was almost saturated after LMSP for 2 h. The highest relative density was determined to be 88.5 ± 0.8% (Fig. 2b). With the optimized uniaxial pressure of 800 MPa and a sintering time of 2 h, the HAP/ZrO_2 mixed nanoparticles with various amounts of ZrO_2 were densified. The relative density of the HAP matrix exhibited the highest value of 89.3 ± 0.6%, while the relative densities of the composites continuously decreased to 88.5 ± 0.8%, 88.3 ± 1.1%, 86.6 ± 1.1%, and 85.4 ± 1.0% as the amount of ZrO_2 increased from 5 to 20 vol% (Fig. 2c and Table S1). This decrease could result from the influence of ZrO_2, which has a poor bioactivity compared to HAP[27] because the densification mechanism in this study is predicated on the precipitation generated through the apatite formation reaction induced by the SBF solution, which fills the void spaces between particles. In LMSP, the interaction between HAP nanoparticles, ZrO_2 nanoparticles, and SBF is complex due to small amount of SBF solution and the environment of pressing and heating. During mixing and pressing, the HAP/ZrO_2 powder with SBF may induce partial dissolution of HAP nanoparticles due to mechanochemical effects[22,23]. This dissolution can increase the pH of the SBF by releasing OH^- ions, potentially initiating the heterogeneous precipitation of calcium phosphate phase such as amorphous calcium phosphate on the surfaces of HAP. However, while the pressing is maintained, the temperature rapidly increases to the target temperature of 130 °C, leading to a decrease in the pH of the SBF[35,36]. Once the temperature exceeds 100 °C and is maintained at 130 °C during sintering, the solubility product of HAP decreases[37], while evaporation of the SBF occurs due to the open system configuration of the LMSP process. With the small amount of SBF added and its supersaturated nature, precipitation from SBF becomes dominant, leading to accelerated formation of apatite-like phases, thereby promoting densification. Under a stoichiometric perspective and assuming complete conversion to HAP, the theoretical amount of HAP precipitate from the added SBF (0.08 g) was calculated based on HPO_4^{2-} ions concentration, which is amount of $K_2HPO_4{\cdot}3H_2O$ contained in SBF, using the following formula[36]:

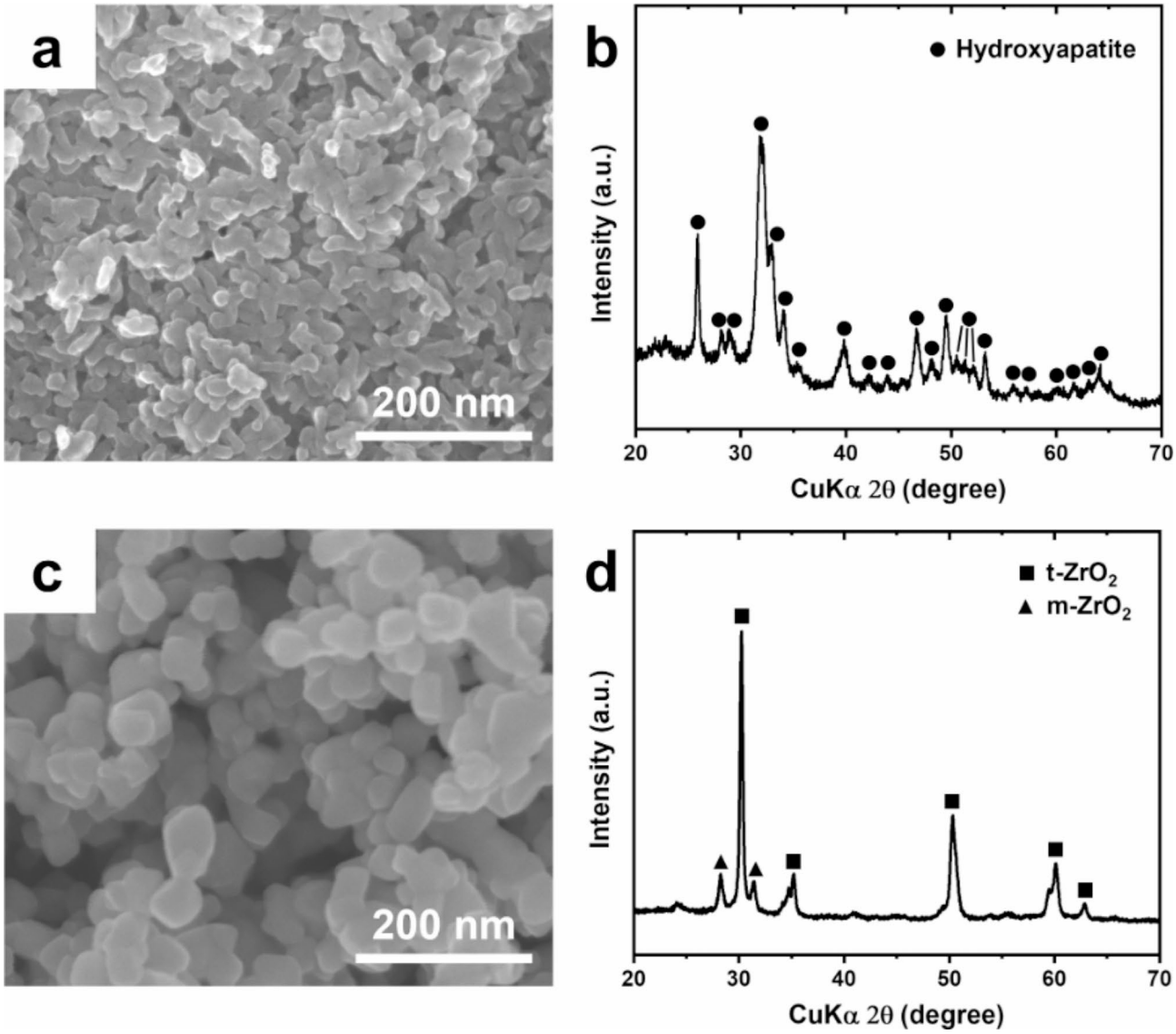

Fig. 1. (**a**) SEM image and (**b**) XRD pattern of the synthesized HAP nanoparticles and (**c**) SEM image and (**d**) XRD pattern of ZrO_2 nanoparticles.

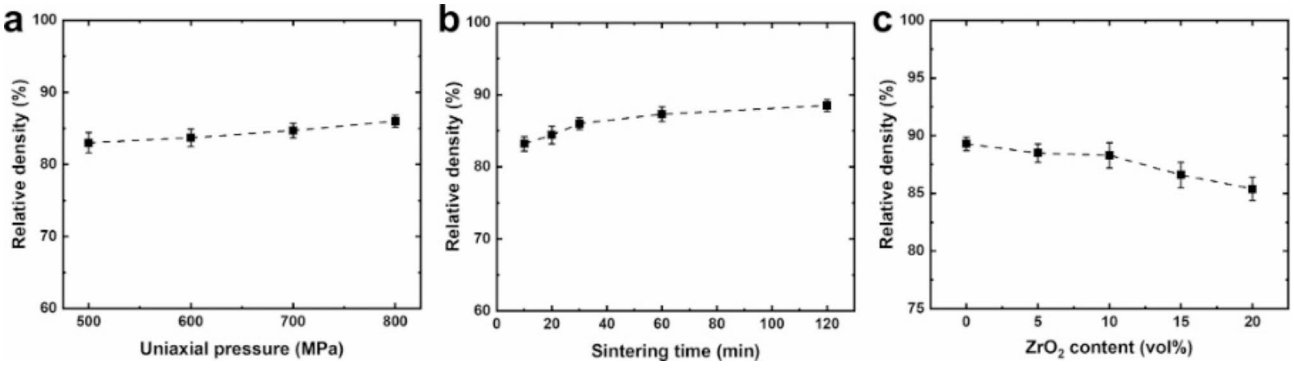

Fig. 2. Relative densities of (**a**) HAP/5 vol% ZrO_2 composites prepared at 130 °C for 30 min under various uniaxial pressures, (**b**) HAP/5 vol% ZrO_2 composites prepared at 130 °C under 800 MPa for different sintering times, and (c) HAP/ZrO_2 composites prepared at 130 °C under 800 MPa for 2 h with varying ZrO_2 content.

$$10Ca^{2+} + 6HPO_4^{2-} + 2H_2O \rightarrow Ca_{10}(PO_4)_6(OH)_2 + 8H^+ \quad (3)$$

From this, the amount of precipitation was determined to be 0.0134 mg. However, in practice, the actual amount may be higher because structural substitution of carbonate ions or cations may result in the formation of calcium-deficient apatite. Furthermore, dissolution-reprecipitation of HAP might affect the total precipitation amount.

Considering the above factors, the influence of precipitation from SBF is believed to be particularly dominant due to the immediate heating after the pressing in the dissolution/reprecipitation process of LMSP. Based on the above mechanism, it can be inferred that the precipitates from SBF may not interact as well with ZrO_2 nanoparticles as with HAP nanoparticles. Additionally, The SBF solution may have difficulty penetrating agglomerated ZrO_2 particles, hindering precipitate formation between them, which could result in decreased relative density of the HAP/ZrO_2 composite as ZrO_2 content increases. However, given the sintering temperature of 130 °C, these relative densities exceeding 90% represent significantly high values compared to those typically achieved in conventional sintering processes[38].

As shown in Fig. 3, fracture surfaces of HAP/ZrO_2 composites exhibited dense microstructures, aligning well with the results of relative density. In the range of 5 to 10 vol% of ZrO_2, despite the presence of a few residual pores, the connection between HAP and ZrO_2 nanoparticles was observed, possibly resulting from the precipitation of a new HAP phase, as discussed in our previous studies[25,26]. Particularly, as a microstructural feature, the densified HAP nanoparticles filled the spaces between the ZrO_2 nanoparticles or covered them, leading to the densification. On the other hand, as the volume fraction of ZrO_2 increased up to 20 vol%, separated ZrO_2 particles were significantly observed on the fracture surfaces. For further investigation, we also prepared the bulk calcia-stabilized ZrO_2 without HAP nanoparticles prepared using LMSP with 20 wt% SBF at 130 °C under the uniaxial pressure of 800 MPa for 120 min. However, the sample was cracked immediately after removal from the mold due to probably weak bonding between the particles (Fig. S1). This can be inferred that as the volume fraction of ZrO_2, known for its challenge in precipitating calcium phosphate phases through

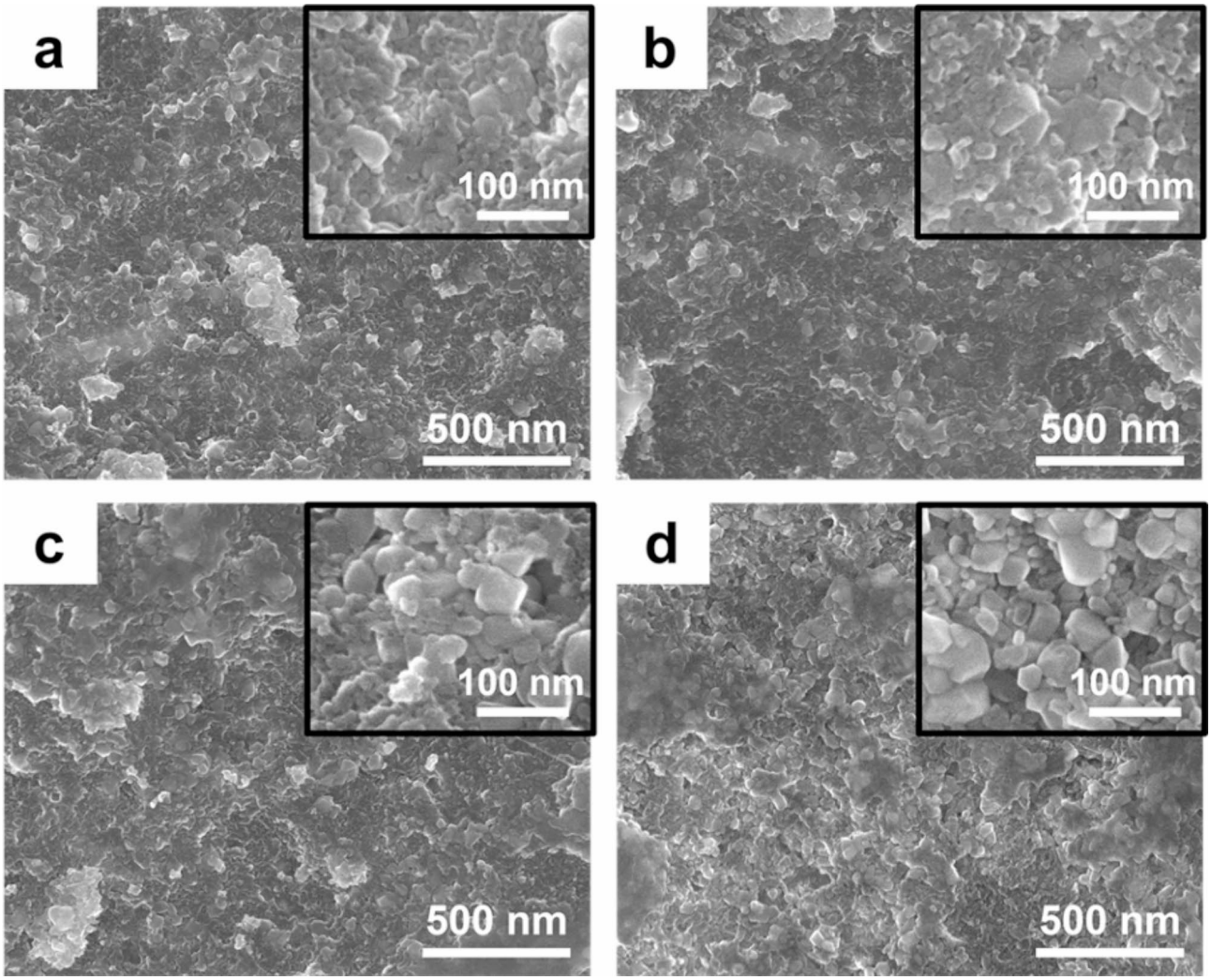

Fig. 3. Fracture surfaces of HAP/ZrO_2 composites prepared at 130 °C under 800 MPa for 2 h with (**a**) 5, (**b**) 10, (**c**) 15, and (**d**) 20 vol% ZrO_2.

a reaction with the SBF solution, increased within the composites, more unreacted and unconnected particles accumulated. Additionally, this resulted in the formation of pores and vacant areas, thereby leading to a decrease in relative density.

To observe the distribution of grains and grain boundaries between HAP and ZrO_2, HAP/ZrO_2 composites with 10 vol% ZrO_2 were examined by TEM and TEM-EDX analysis (Fig. 4). As shown in Fig. 4a–c, HAP and ZrO_2 grains were clearly distinguished by the TEM-EDX mapping analysis. Larger ZrO_2 grains were dispersed in the HAP matrix, indicating a good distribution. This microstructural feature was also observed in the TEM image of the composite (Fig. 4d). In addition, a triple point of HAP and ZrO_2 grains was observed, representing dense microstructural features (Fig. 4e). Although several pores existed at the grain boundaries (Fig. 4a, d), most grain boundary phases were crystallized, exhibiting lattice fringes, as shown in high-resolution TEM images (Fig. 4e, f). Notably, t-ZrO_2 as well as m-ZrO_2 grains were observed. These large grains were well contacted to small HAP grains. In this regard, the precipitate, probably the HAP phase, was distributed at the grain boundaries and connected HAP with ZrO_2 grains through precipitation from SBF in the dense regions of the composites during LMSP.

Phase analysis of HAP/ZrO_2 composites

The phase structures of the HAP/ZrO_2 composites were examined against the sintering times, uniaxial pressures, and ZrO_2 contents using XRD (Fig. 5). Across all XRD measurements, a decrease in the XRD peak intensity for the (002) plane at $2\theta = 25.9°$ was observed, while the peak intensity of the (300) plane at $2\theta = 33.0°$ showed an increase, when compared to the XRD pattern of HAP nanoparticles (Fig. 1). This alteration is attributed to the orientation of granular HAP nanoparticles along the vertical axis of the applied uniaxial pressure, resulting in a non-uniform alignment of the c-axis[26]. As shown in Fig. 5a, for the HAP/ZrO_2 composites with 5 vol% ZrO_2 with different sintering times, all recorded XRD peaks exclusively represented HAP and ZrO_2 phases, without the formation of decomposed phases observed in a high-temperature sintering process[16–18]. Notably, XRD peaks corresponding to m-ZrO_2 (PDF no. 00–037–1484) were observed at $2\theta = 28.3$, 31.4, and 54.3° following LMSP, while the main peak for t-ZrO_2 (PDF no. 00–079–1769) at $2\theta = 30.2°$ remained with a higher intensity. Compared to the XRD pattern of raw ZrO_2 nanoparticles (Fig. 1d), the intensities of these XRD peaks related to m-ZrO_2 increased. For further investigation of the transformation to the monoclinic phase, the MIR was calculated based on the XRD results. As a result, the MIR of raw ZrO_2 nanoparticles was determined to be 15.8%, while the MIR increased to 30.5% for the HAP/ZrO_2 composites with 5 vol% ZrO_2 sintered for 2 h. Interestingly, the MIRs of the HAP/ZrO_2 composites with 5 vol% ZrO_2 and different sintering times exhibited similar values, which agreed with the XRD observation (Fig. 5a, b). Additionally, the XRD patterns and MIRs of the HAP/ZrO_2 composites with 5 vol% ZrO_2 with increasing uniaxial pressure from 200 to 800 MPa exhibited similar aspects and values, respectively (Fig. 5c, d). In addition, the bulk calcia-stabilized ZrO_2 without HAP nanoparticles, prepared using LMSP, was examined by XRD analysis (Fig. S2). In this case, the intensities of these XRD peaks related to m-ZrO_2

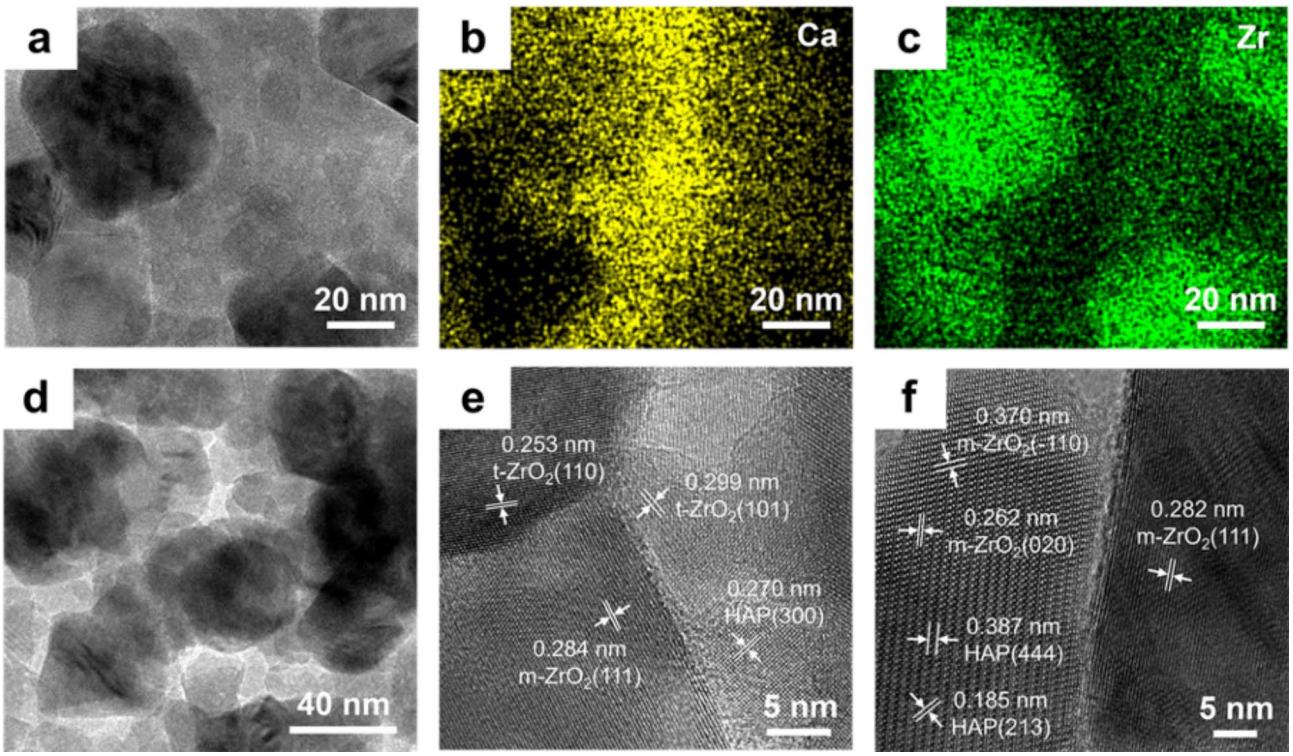

Fig. 4. (**a**)–(**c**) TEM-EDX mapping images, (**d**) TEM image, and (**e**, **f**) high-resolution TEM images of HAP/ZrO_2 composites with 10 vol% ZrO_2 prepared at 130 °C under 800 MPa for 2 h.

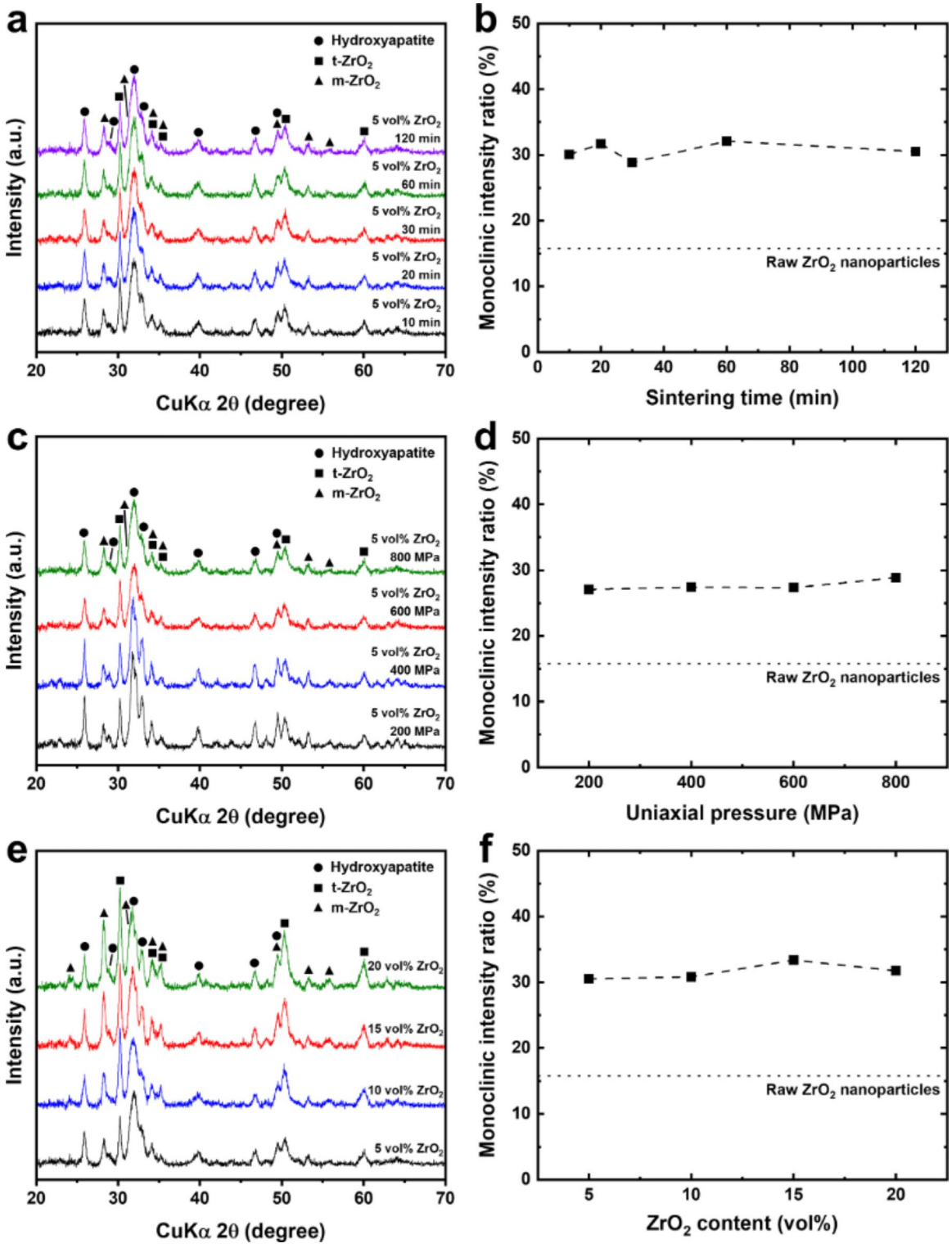

Fig. 5. XRD patterns and MIR calculation results of (**a**, **b**) HAP/5 vol% ZrO_2 composites prepared at 130 °C under 800 MPa with different sintering times, (**c**, **d**) HAP/5 vol% ZrO_2 composites prepared at 130 °C for 30 min under various uniaxial pressures, and (**e**, **f**) HAP/ZrO_2 composites prepared at 130 °C under 800 MPa for 120 min with different ZrO_2 contents. The dotted line represents the MIR calculation result of raw ZrO_2 nanoparticles.

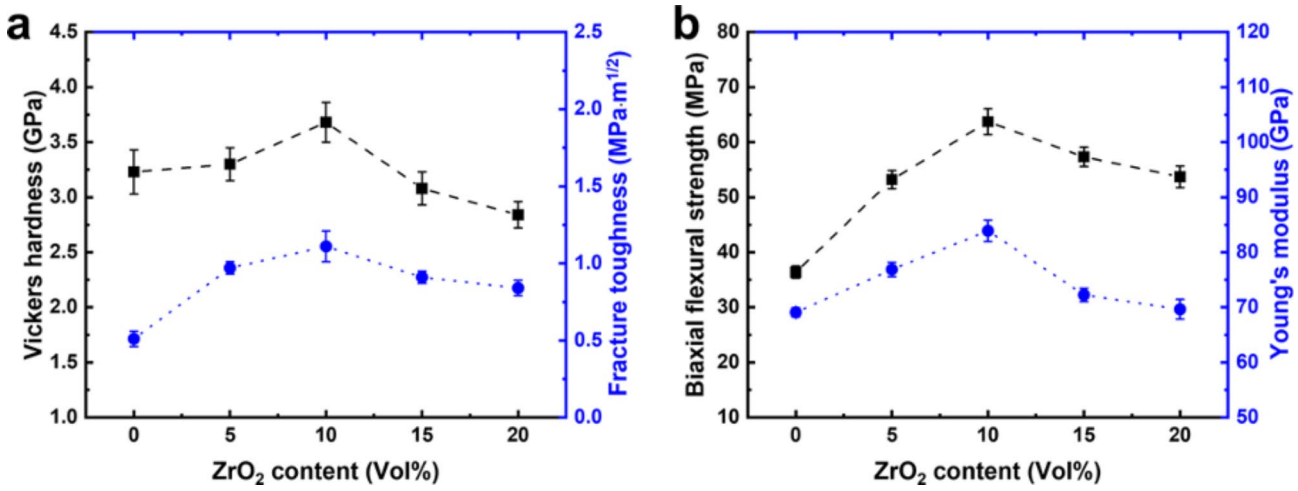

Fig. 6. (**a**) Vickers hardnesses, fracture toughnesss, (**b**) biaxial flexural strengths, and Young's moduli of the HAP/ZrO_2 composites prepared at 130 °C under 800 MPa for 2 h with varying ZrO_2 content.

Samples	Mechanical properties			
	Vickers hardness (GPa)	Fracture toughness (MPa·m$^{1/2}$)	Biaxial flexural strength (MPa)	Young's modulus (GPa)
Pure HAP (0 vol% ZrO_2)	3.23 ± 0.36	0.51 ± 0.05	36.39 ± 1.09	69.09 ± 0.83
5 vol% ZrO_2	3.30 ± 0.15	0.97 ± 0.04	53.21 ± 1.65	76.88 ± 1.32
10 vol% ZrO_2	3.68 ± 0.18	1.11 ± 0.10	63.72 ± 2.35	83.91 ± 1.93
15 vol% ZrO_2	3.08 ± 0.15	0.91 ± 0.04	57.33 ± 1.75	72.26 ± 1.23
20 vol% ZrO_2	2.84 ± 0.12	0.84 ± 0.05	57.33 ± 1.75	69.66 ± 1.77

Table 2. Mechanical propertiesss of HAP/ZrO_2 composites prepared at 130 °C under 800 MPa for 2 h varying ZrO_2 content.

also increased compared to those of raw ZrO_2 nanoparticles, and the MIR value was determined to be 31.2%, which is comparable to the value presented in Fig. 5. This suggests that the sintering time, uniaxial pressure, and the presence of HAP phase would not affect the phase transformation to monoclinic.

As shown in Fig. 5e and f, XRD patterns and MIRs for HAP/ZrO_2 composites with different amounts of ZrO_2 were also investigated. The increase in ZrO_2 content led to higher peak intensities of both m- and t-ZrO_2, resulting in similar MIRs at different ZrO_2 amounts. Despite changes in parameters such as the sintering time, uniaxial pressure, and ZrO_2 content, the MIR remained consistent at approximately 30%. From these results, we could assume that the transformation to the monoclinic phase may be influenced by the SBF solution under LMSP environment. During pressing and heating in LMSP, the surfaces of raw ZrO_2 nanoparticles could be modified and activated, leading to formation of Zr-OH groups on their surfaces by the SBF solution, which serve as effective sites for apatite nucleation[39,40]. This reaction, particularly at grain boundaries, can induce the tetragonal-to-monoclinic transformation. Additionally, during LMSP, the evaporation of SBF solution generates water vapor, potentially promoting the formation of Zr-OH groups accompanied with a partial dissolution at the surfaces of ZrO_2 nanoparticles, leading to phase transformation[41]. After the SBF solution is almost completely evaporated during LMSP, the Zr-OH formation reaction may not further occur. It can be regarded that a constant level of monoclinic ratio was maintained regardless of other parameters such as the sintering time, uniaxial pressure, and ZrO_2 content.

Mechanical properties of HAP/ZrO_2 composites

To evaluate mechanical properties of HAP/ZrO_2 composites with various amounts of ZrO_2, the Vickers hardness, fracture toughness, biaxial flexural strength, and Young's modulus were measured (Fig. 6; Table 2).

As shown in Fig. 6, all mechanical properties of the composites against the volume fraction of ZrO_2 exhibited a similar changing trend. At ZrO_2 contents of 0 to 10 vol%, all mechanical property values increased. The Vickers hardness and fracture toughness were improved from 3.23 ± 0.36 to 3.68 ± 0.18 GPa and from 0.51 ± 0.05 to 1.11 ± 0.10 MPa·m$^{1/2}$, respectively (Fig. 6a). Moreover, the biaxial flexural strength and Young's modulus increased from 36.39 ± 1.09 to 63.72 ± 2.35 MPa and from 69.09 ± 0.83 to 83.91 ± 1.93 GPa, respectively (Fig. 6b). This enhancement can be attributed to the good densification and toughening mechanism with the incorporation of ZrO_2 nanoparticles into the composites. However, in the range of 10 to 20 vol% of ZrO_2, all mechanical properties exhibited a sudden decreasing trend despite the increase in the amount of ZrO_2 in the

composites. As shown in Figs. 2 and 3, the relative density further decreased, and increases in the contents of pores and vacant areas on the fracture surfaces were observed within this range of ZrO_2 content, resulting in degradations of the mechanical properties. Compared to the conventional sintering techniques[16,19,38], the possible incorporation amount of ZrO_2 to enhance mechanical properties was limited in this study. This limitation could be attributed to the insufficient dissolution–precipitation at ZrO_2 nanoparticles. For further enhancements in the mechanical properties, it will be necessary to explore strategies to enhance the reactivity of ZrO_2 and optimize the dissolution–reprecipitation process with the SBF solution during LMSP in our future studies. Nevertheless, significant improvements in mechanical properties of the composites were achieved at 10 vol% of ZrO_2.

Consequently, HAP/ZrO_2 composites with improved mechanical properties could be obtained at an extremely lower sintering temperature (130 °C), approximately 1000 °C lower than those (1200–1500 °C) in previous studies utilizing other sintering techniques[10,15–21,38,42]. Moreover, owing to the low sintering temperature, HAP did not undergo the phase decomposition into β-TCP, $Ca_{10}(PO_4)_6O$, and CaO during the sintering process. Based on these results, LMSP is promising for densification of various biological inorganic materials as well as the incorporation of diverse reinforcing materials leading to further enhancements in their properties.

Conclusion

HAP/ZrO_2 nanocomposites with enhanced mechanical properties were successfully fabricated via LMSP utilizing the SBF solution. Under the LMSP environment inducing the biomineralization, HAP and ZrO_2 nanoparticles were well densified at a super-low sintering temperature of 130 °C and exhibited a high relative density (approximately 88%) at 10 vol% of ZrO_2. Additionally, HAP and ZrO_2 nanoparticles were well distributed, almost no pores were observed between the HAP and ZrO_2 grains, and lattice fringes were clearly observed in their grain boundaries. However, degradations in relative density and mechanical properties were observed at ZrO_2 contents of 10 to 20 vol% due to the increasing amount of ZrO_2, which undergoes limited dissolution–precipitation under LMSP conditions. Overall, the HAP/ZrO_2 composites with 10 vol% ZrO_2 at the sintering temperature of only 130 °C exhibited enhanced mechanical properties, compared to those of the pure HAP matrix. We believe that LMSP is a promising low-energy and eco-friendly technique that can be utilized not only for the densification of various bioactive materials but also for enhancements in their properties through combinations with reinforcing materials. This innovative approach has a potential to increase the performances of bioactive materials in diverse applications.

Data availability

The datasets used and/or analyzed in the current study are available from the corresponding author upon reasonable request.

Received: 22 July 2024; Accepted: 1 January 2025
Published online: 20 January 2025

References

1. Bagambisa, F. B., Joos, U. & Schilli, W. Mechanisms and structure of the bond between bone and hydroxyapatite ceramics. *J. Biomed. Mater. Res.* **27**, 1047–1055 (1993).
2. Zhou, H. & Lee, J. Nanoscale hydroxyapatite particles for bone tissue engineering. *Acta Biomater.* **7**, 2769–2781 (2011).
3. Ripamonti, U., Roden, L. C. & Renton, L. F. Osteoinductive hydroxyapatite-coated titanium implants. *Biomater.* **33**, 3813–3823 (2012).
4. Li, S. *et al.* Porous polyetheretherketone-hydroxyapatite composite: a candidate material for orthopedic implant. *Compos. Commun.* **28**, 100908 (2021).
5. Fan, X. Preparation and performance of hydroxyapatite/Ti porous biocomposite scaffolds. *Ceram. Int.* **45**, 16466–16469 (2019).
6. Wu, Y. *et al.* Comparative studies on micromechanical properties and biological performances in hydroxyapatite ceramics with micro/nanocrystalline. *J. Am. Ceram. Soc.* **105**, 742–756 (2022).
7. Katti, K. S. Biomaterials in total joint replacement. *Colloids Surf. B* **39**, 133–142 (2004).
8. Balamurugan, A., Rajeswari, S., Balossier, G., Rebelo, A. H. S. & Ferreira, J. M. F. Corrosion aspects of metallic implants - an overview. *Mater. Corros.* **59**, 855–869 (2008).
9. Epure, L. M., Dimitrievska, S., Merhi, Y. & Yahia, L. The effect of varying Al_2O_3 percentage in hydroxyapatite/Al_2O_3 composite materials: morphological, chemical and cytotoxic evaluation. *J. Biomed. Mater. Res.* A **83**, 1009–1023 (2007).
10. Rapacz-Kmita, A., Ślósarczyk, A. & Paszkiewicz, Z. Mechanical properties of HAp-ZrO_2 composites. *J. Eur. Ceram. Soc.* **26**, 1481–1488 (2006).
11. Etyemez, A. Structural, physical, and mechanical properties of the TiO_2 added hydroxyapatite composites. *Open Chem.* **20**, 272–276 (2022).
12. Lin, H., Yin, C. & Mo, A. Zirconia based dental biomaterials: structure, mechanical properties, biocompatibility, surface modification, and applications as implant. *Front. Dent. Med.* **2**, 689198 (2021).
13. Hanawa, T. Zirconia versus titanium in dentistry: a review. *Dent. Mater. J.* **39**, 24–36 (2020).
14. Wang, J. *et al.* Good biocompatibility and sintering properties of zirconia nanoparticles synthesized via vapor-phase hydrolysis. *Sci. Rep.* **6**, 35020 (2016).
15. Kantana, W. *et al.* Properties of hydroxyapatite/zirconium oxide nanocomposites. *Ceram. Int.* **39**, S379–S382 (2013).
16. Castkova, K. *et al.* Synthesis of Ca,Y-zirconia/hydroxyapatite nanoparticles and composites. *J. Eur. Ceram. Soc.* **36**, 2903–2912 (2016).
17. Curran, D. J., Fleming, T. J., Towler, M. R. & Hampshire, S. Mechanical properties of hydroxyapatite-zirconia compacts sintered by two different sintering methods. *J. Mater. Sci. Mater. Med.* **21**, 1109–1120 (2010).
18. Evis, Z. & Doremus, R. H. Hot-pressed hydroxylapatite/monoclinic zirconia composites with improved mechanical properties. *J. Mater. Sci.* **42**, 2426–2431 (2007).
19. Kumar, V. A., Rama Murty Raju, P., Ramanaiah, N. & Siriyala, R. Effect of ZrO_2 content on the mechanical properties and microstructure of HAp/ZrO_2 nanocomposites. *Ceram. Int.* **44**, 10345–10351 (2018).
20. Li, W. & Gao, L. Fabrication of HAp-ZrO_2 (3Y) nano-composite by SPS. *Biomater.* **24**, 937–940 (2003).

21. Auger, M. A. *et al*. Mechanical characteristics of porous hydroxyapatite/oxide composites produced by post-sintering hot isostatic pressing. *Ceram. Int*. **35**, 2373–2380 (2009).
22. Guo, H., Baker, A., Guo, J. & Randall, C. A. Cold sintering process: a novel technique for low-temperature ceramic processing of ferroelectrics. *J. Am. Ceram. Soc*. **99**, 3489–3507 (2016).
23. Guo, H., Baker, A., Guo, J. & Randall, C. A. Protocol for ultralow-temperature ceramic sintering: an integration of nanotechnology and the cold sintering process. *ACS Nano* **10**, 10606–10614 (2016).
24. Maria, J. P. *et al*. Cold sintering: current status and prospects. *J. Mater. Res*. **32**, 3205–3218 (2017).
25. Seo, Y., Goto, T., Cho, S. & Sekino, T. Crystallization behavior of the low-temperature mineralization sintering process for glass nanoparticles. *Materials* **13**, 3281 (2020).
26. Seo, Y., Goto, T., Cho, S. & Sekino, T. Densification of transparent hydroxyapatite ceramics via cold sintering process combined with biomineralization. *J. Eur. Ceram. Soc*. **44**, 4285–4293 (2024).
27. Liu, X., Huang, A., Ding, C. & Chu, P. K. Bioactivity and cytocompatibility of zirconia (ZrO_2) films fabricated by cathodic arc deposition. *Biomater*. **27**, 3904–3911 (2006).
28. Bakan, F., Laçin, O. & Sarac, H. A novel low temperature sol-gel synthesis process for thermally stable nano crystalline hydroxyapatite. *Powder Technol*. **233**, 295–302 (2013).
29. Wang, J. & Shaw, L. L. Morphology-enhanced low-temperature sintering of nanocrystalline hydroxyapatite. *Adv. Mater*. **19**, 2364–2369 (2007).
30. Kokubo, T., Kushitani, H., Sakka, S., Kitsugi, T. & Yamamuro, T. Solutions able to reproduce in vivo surface-structure changes in bioactive glass-ceramic A-W[3]. *J. Biomed. Mater. Res*. **24**, 721–734 (1990).
31. Toraya, H., Yoshimura, M. & Somiya, S. Calibration curve for quantitative analysis of the monoclinic-tetragonal ZrO_2 system by X-ray diffraction. *J. Am. Ceram. Soc*. **67**, C-119–C-121 (1984).
32. Nobuta, Y. *et al*. Crystallization of nanostructured ZrO_2 phase in borosilicate glass: impact of Al_2O_3 on tetragonal-to-monoclinic phase transformation. *J. Non-Cryst. Solids* **501**, 49–54 (2018).
33. Niihara, K. A fracture mechanics analysis of indentation-induced Palmqvist crack in ceramics. *J. Mater. Sci. Lett*. **2**, 221–223 (1983).
34. Galotta, A. & Sglavo, V. M. The cold sintering process: a review on processing features, densification mechanisms and perspectives. *J. Eur. Ceram. Soc*. **41**, 1–17 (2021).
35. Müller, L., Müller, F. A. Preparation of SBF with different HCO_3^- content and its influence on the composition of biomimetic apatites. *Acta Biomater.* **2**, 181–189 (2006).
36. Prywer, J., Kozanecki, M., Mielniczek-Brzóska, E., Torzewska, A. Solid phases precipitating in artificial urine in the absence and presence of bacteria proteus mirabilis–A contribution to the understanding of infectious urinary stone formation, *Crystals* **8**, 164 (2018).
37. Tamura, M., Endo, K., Maida, T., Ohno, H. Hydroxyapatite film coating by thermally induced liquid-phase deposition method for titanium implants. *Dent. Mater. J*. **25**, 32–38 (2006).
38. Zhang, J. *et al*. Fabrication of hydroxyapatite-zirconia composites for orthopedic applications. *J. Am. Ceram. Soc*. **89**, 3348–3355 (2006).
39. Dehestani, M., Ilver, L. & Adolfsson, E. Enhancing the bioactivity of zirconia and zirconia composites by surface modification. *J. Biomed. Mater. Res. B* **100 B**, 832–840 (2012).
40. Uchida, M., Kim, H. M., Kokubo, T., Miyaji, F. & Nakamura, T. Bonelike apatite formation induced on zirconia gel in a simulated body fluid and its modified solutions. *J. Am. Ceram. Soc*. **84**, 2041–2044 (2001).
41. Sato, T. & Shimada, M. Transformation of yttria-doped tetragonal ZrO_2 polycrystals by annealing in water. *J. Am. Ceram. Soc*. **68**, 356–356 (1985).
42. Volceanov, A., Volceanov, E. & Stoleriu, S. Hydroxiapatite-zirconia composites for biomedical applications. *J. Optoelectron. Adv. Mater*. **8**, 585–588 (2006).

Acknowledgements

This work was supported by JSPS Grant-in-Aid for Early-Career Scientists [grant number JP22K14476] and the research project of "Crossover Alliance to Create the Future with People, Intelligence and Materials" from MEXT, Japan. The calcia-stabilized ZrO_2 nanoparticles used in this study were provided by Daiichi Kigenso Kagaku Kogyo Co., Ltd. TEM observations were performed at the Comprehensive Analysis Center, SANKEN, Osaka University, Japan. The authors are grateful to Mr. Y. Murakami (Osaka University, Japan) for his technical support in TEM observations.

Author contributions

Y.S.: Conceptualization, Methodology, Formal analysis, Investigation, Writing - Original Draft, Writing - Review & Editing, Funding acquisition. N.S.: Investigation, Formal analysis. T.G.: Methodology, Investigation. S.C.: Formal analysis, Investigation. S.T.: Conceptualization, Methodology, Supervision. All authors reviewed the manuscript.

Declarations

Competing interests

The authors declare no competing interests.

Additional information

Supplementary Information The online version contains supplementary material available at https://doi.org/10.1038/s41598-025-85116-w.

Correspondence and requests for materials should be addressed to Y.S. or T.S.